Received: 10 February 2016 | Revised: 15 May 2017 | Accepted: 24 May 2017

DOI: 10.1002/rob.21731

FIELD REPORT

WILEY

Autonomous car driving by a humanoid robot

Antonio Paolillo[1,2] | **Pierre Gergondet**[2] | **Andrea Cherubini**[1] | **Marilena Vendittelli**[3] | **Abderrahmane Kheddar**[1,2]

[1]CNRS-UM LIRMM, Montpellier, France

[2]CNRS-AIST JRL UMI3218/RL, Tsukuba, Japan

[3]DIAG, Sapienza Università di Roma, Roma, Italy

Correspondence
Antonio Paolillo, CNRS-UM LIRMM 161 Rue Ada, 34090 Montpellier.
Email: paolillo@lirmm.fr

Abstract

Enabling a humanoid robot to drive a car requires the development of a set of basic primitive actions. These include walking to the vehicle, manually controlling its commands (e.g., ignition, gas pedal, and steering) and moving with the whole body to ingress/egress the car. We present a sensor-based reactive framework for realizing the central part of the complete task, consisting of driving the car along unknown roads. The proposed framework provides three driving strategies by which a human supervisor can teleoperate the car or give the robot full or partial control of the car. A visual servoing scheme uses features of the road image to provide the reference angle for the steering wheel to drive the car at the center of the road. Simultaneously, a Kalman filter merges optical flow and accelerometer measurements to estimate the car linear velocity and correspondingly compute the gas pedal command for driving at a desired speed. The steering wheel and gas pedal reference are sent to the robot control to achieve the driving task with the humanoid. We present results from a driving experience with a real car and the humanoid robot HRP-2Kai. Part of the framework has been used to perform the driving task at the DARPA Robotics Challenge.

KEYWORDS

autonomous driving, humanoid robots, visual control

1 | INTRODUCTION

The potential of humanoid robots in the context of disaster has been exhibited recently at the DARPA Robotics Challenge (DRC), where robots performed complex locomotion and manipulation tasks.[1] The DRC has shown that humanoids should be capable of operating machinery, originally designed for humans. The DRC utility car driving task is a good illustration of the complexity of such tasks.

Worldwide, to have the right to drive a vehicle, one needs to be delivered a license, requiring months of practice, followed by an examination test. To make a robot drive in similar conditions, the perception and control algorithms should reproduce the human-driving skills.

If the vehicle can neither be customized nor automated, it is more convenient to think of a robot in terms of anthropomorphic design. A driving robot must have motion capabilities for operations such as reaching the vehicle, entering it, sitting in a stable posture, controlling its commands (e.g., ignition, steering wheel, pedals), and finally egressing it. All these skills can be seen as action templates, to be tailored to each vehicle and robot, and, more importantly, to be properly combined and sequenced to achieve driving tasks.

Noticeable research is currently made to automate the driving operation of unmanned vehicles, with the ultimate goal of reproducing the tasks usually performed by human drivers,[2–4] by relying on visual sensors.[5–7] The success of the DARPA Urban Challenges[8,9] and the impressive demonstrations made by Google[10] have heightened expectations that autonomous cars will very soon be able to operate in urban environments. Considering this, why bother making a robot drive a car, if the car can make its way without a robot? Although both approaches are not exclusive, this is certainly a legitimate question.

One possible answer springs from the complexity of autonomous cars, which host a *distributed robot*, with various sensors and actuators controlling the different tasks. With a *centralized robot*, such embedded devices can be removed from the car. The reader may also wonder when should a *centralized* robot be preferred to a *distributed* one, that is, a fully automated car?

We answer this question through concrete application examples. In the DRC,[11] one of the eight tasks that robot must overtake is driving a utility vehicle. The reason is that in disaster situations, the intervention robot must operate vehicles—usually driven by humans—to transport tools, debris, etc. Once the vehicle reaches the intervention area, the robot should execute other tasks (e.g., turning a valve, operating a drill). Without a humanoid, these tasks can be hardly achieved by a unique system. Moreover, the robot should operate cranks or other tools attached to the vehicle.[12,13] A second demand comes from the car manufacturing industry.[14] In fact, current crash-test dummies are passive and nonactuated. Instead, in crash situations, real humans perform

protective motions and stiffen their body, all behaviors that are programmable on humanoid robots. Therefore, robotic crash-test dummies would be more realistic in reproducing typical human behaviors.

These applications, along with the DRC itself, and with the related algorithmic questions, motivate the interest for developing a robot driver. However, this requires the solution of an unprecedented "humanoid-in-the-loop" control problem. In our work, we successfully address this and demonstrate the capability of a humanoid robot to drive a real car. This work is based on preliminary results carried out with the HRP-4 robot, driving a simulated car.[15] Here, we add new features to that framework and present experiments with humanoid HRP-2Kai driving a real car outdoor on an unknown road.

The proposed framework presents the following main features:

- car steering control, to keep the car at a defined center of the road;
- car velocity control, to drive the car at a desired speed;
- admittance control, to ensure safe manipulation of the steering wheel;
- three different driving strategies, allowing intervention or supervision of a human operator, in a smooth shared autonomy manner.

The modularity of the approach allows to easily enable or disable each of the modules that compose the framework. Furthermore, to achieve the driving task, we propose to use only standard sensors for a common full-size humanoid robot, that is, a monocular camera mounted on the head of the robot, the inertial measurement unit (IMU) in the chest, and the force sensors at the wrists. Finally, the approach being purely reactive, it does not need any a priori knowledge of the environment. As a result, the framework allows—under certain assumptions—to make the robot drive along a previously unknown road.

The paper organization reflects the schematic description of the approach given in Section 2, at the end of which we also provide a short description of the paper sections.

2 | PROBLEM FORMULATION AND PROPOSED APPROACH

The objective of this work is to enable a humanoid robot to autonomously drive a car at the center of an unknown road at a desired velocity. More specifically, we focus on the driving task and, therefore, consider the robot sitting in the car, already in a correct driving posture.

Most of the existing approaches have achieved this goal by relying on teleoperation.[16–22] Supervisory steering and gas commands are sent to the robot to drive the car in Karumanchi et al.[23]; DeDonato and colleagues[24] propose a hybrid solution, with teleoperated steering and autonomous speed control. The velocity of the car, estimated with stereo cameras, is fed back to a proportional integral (PI) controller, whereas light imaging, detection, and ranging (LIDAR), IMU, and visual odometry data support the operator during the steering procedures. In Kumagai et al.,[25] the gas pedal is teleoperated and a local planner, using robot kinematics for vehicle path estimation, and point cloud data for obstacle detection, enables autonomous steering. An impedance system is used to ensure safe manipulation of the steering wheel.

Other researchers have proposed fully autonomous solutions. For instance, in Jeong et al.,[26] autonomous robot driving is achieved by following the proper trajectory among obstacles, detected with laser measurements. LIDAR scans are used in Rasmussen et al.[27] to plan a path for the car, whereas the velocity is estimated with a visual odometry module. The operation of the steering wheel and gas pedal is realized with simple controllers.

We propose a reactive approach for autonomous driving that relies solely on standard humanoids sensor equipment, thus making it independent from the vehicle sensorial capabilities and does not require expensive data elaboration for building local representations of the environment and planning safe paths. In particular, we use data from the robot on-board camera and IMU to close the autonomous driver feedback loop. The force measured on the robot wrists is exploited to operate the car steering wheel.

In designing the proposed solution, some simplifying assumptions have been introduced to capture the conceptual structure of the problem without losing generality:

1. The car brake and clutch pedals are not considered, and the driving speed is assumed to be positive and independently controlled through the gas pedal. Hence, the steering wheel and the gas pedals are the only vehicle controls used by the robot for driving.
2. The robot is already in its driving posture on the seat, with one hand on the steering wheel, the foot on the pedal, and the camera pointing the road, with focal axis aligned with the car sagittal plane. The hand grasping configuration is unchanged during operation.
3. The road is assumed to be locally flat, horizontal, straight, and delimited by parallel borders.* Although global convergence can be proved only for straight roads, turns with admissible curvature bounds are also feasible, as shown in the Experimental section. Instead, crossings, traffic lights, and pedestrians are not negotiated, and road signs are not interpreted.

Given these assumptions, we propose the control architecture in Figure 1. The robot sits in the car, with its camera pointing to the road. The acquired images and IMU data are used by two branches of the framework running in parallel: car steering and velocity control. These are described hereby.

The car steering algorithm guarantees that the car is maintained at the center of the road. To this end, the IMU is used to get the camera orientation with respect to the road, whereas an image-processing algorithm detects the road borders (*road detection*). These borders are used to compute the visual features feeding the *steering control* block. Finally, the computed steering wheel reference angle is transformed by the *wheel operation* block into a desired trajectory for the robot hand that is operating the steering wheel. This trajectory can be adjusted by an admittance system, depending on the force exchanged between the robot hand and the steering wheel.

* The assumption on parallel road borders can be relaxed, as proved in Paolillo et al.[28] We maintain the assumption here to keep the description of the controller simpler, as will be shown in Section 5.1.

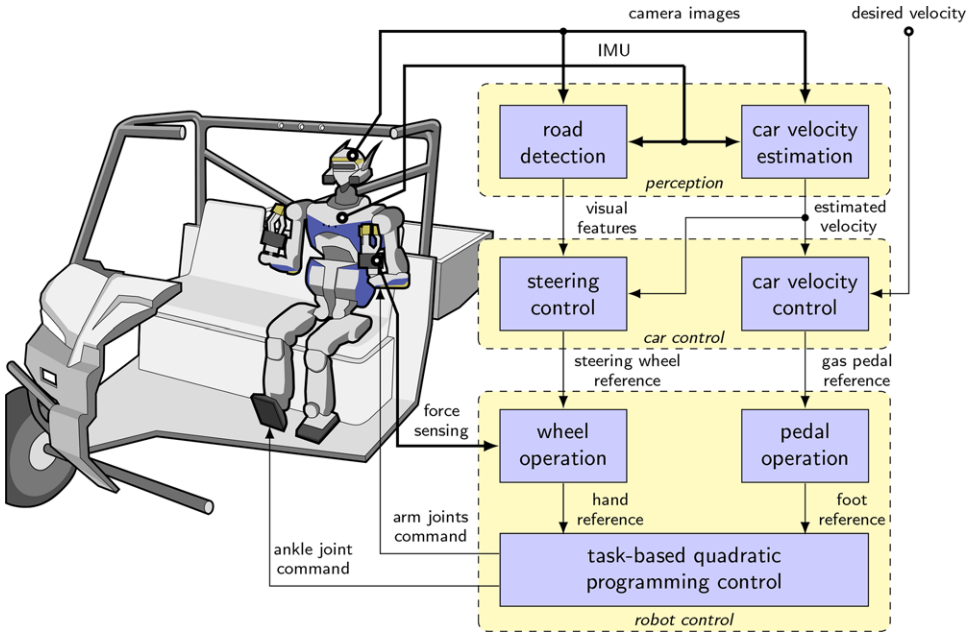

FIGURE 1 Conceptual block diagram of the driving framework

The car velocity control branch aims at making the car progress at a desired speed, through the gas pedal operation by the robot foot. A Kalman filter (KF) fuses visual and inertial data to estimate the velocity of the vehicle (*car velocity estimation*) sent as feedback to the *car velocity control*, which provides the gas pedal reference angle for obtaining the desired velocity. The *pedal operation* block transforms this signal into a reference for the robot foot.

Finally, the reference trajectories for the hand and the foot, respectively, operating the steering wheel and the pedal, are converted into robot postural tasks, by the *task-based quadratic programming (QP) controller*.

The driving framework, as described above, allows a humanoid robot to autonomously drive a car along an unknown road at a desired velocity. We further extend the versatility of our framework by implementing three different "driving modes," to ease human supervision and possible intervention if needed:

- *Autonomous*. Car steering and velocity control are both enabled, as indicated above, and the robot autonomously drives the car without any human aid.
- *Shared-autonomy*. The user remotely operates the robot foot on the pedal and specifies the target in the image for the steering operations.
- *Teleoperated*. Both the robot hand and foot are teleoperated for steering the wheel and the gas pedal operation, respectively. The reference signals are sent to the task-based QP control through a keyboard or joystick. The human uses the robot camera images as visual feedback for driving.

For each of the driving modes, the car steering and velocity controllers are enabled or disabled, as described in Table 1. The human user/supervisor can intervene at any moment during the execution of the driving task, to select one of the three driving modes. The selection, as well as the switching between modes, is done by pushing proper joystick (or keyboard) buttons.

TABLE 1 Driving modes

Driving Mode	Steering Control	Car Velocity Control
Autonomous	Enabled	Enabled
Shared-autonomy	Enabled[a]	Disabled
Teleoperated	Disabled	Disabled

Note: For each mode, the steering and the car velocity control are properly enabled or disabled.
[a]Road detection is assisted by the human.

The framework has a modular structure, as presented in Figure 1. In the following sections, we detail the primitive functionalities required by the autonomous mode, since the shared autonomy and teleoperation modes use a subset of such functionalities.

The rest of paper is organized as follows. Section 3 describes the model used for the car–robot system. Then, the main components of the proposed framework are detailed. Section 4 presents the perception part, that is, the algorithms used to detect the road and to estimate the car velocity. Section 5 deals with car control, that is, how the feedback signals are transformed into references for the steering wheel and for the gas pedal, whereas Section 6 focuses on humanoid control, that is, on the computation of the commands for the robot hand and foot. The experiments carried out with HRP-2Kai are presented in Section 7. Finally, Section 8 concludes the paper and outlines future research perspectives.

3 | MODELING

The design of the steering controller is based on the car kinematic model. This is a reasonable choice since, for nonholonomic systems, it is possible to cancel the dynamic parameters via feedback and to solve the control problem at the velocity level, provided that the velocity

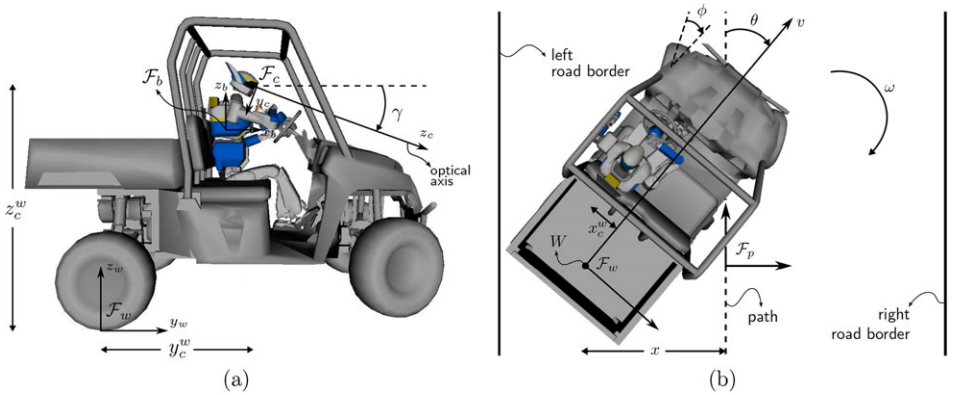

FIGURE 2 Side (a) and top view (b) of a humanoid robot driving a car with relevant variables

issued by the controller is differentiable.[29] To recover the dynamic system control input, it is however necessary to know the exact dynamic model, which is in general not available. Although some approximations are therefore necessary, these do not affect the controller in the considered scenario (low accelerations, flat and horizontal road). Online car dynamic parameter identification could be envisaged and seamlessly integrated in our framework, whenever the above assumptions are not valid. Note, however, that the proposed kinematic controller would remain valid, since it captures the theoretic challenge of driving in the presence of nonholonomic constraints.

To derive the car control model, consider the reference frame $\mathcal{F}_w$ placed on the car rear axle midpoint W, with the y-axis pointing forward, the z-axis upward and the x-axis completing the right-handed frame [see Fig. 2(a)]. The path to be followed is defined as the set of points that maximize the distance from both the left and right road borders. On this path, we consider a tangent Frenet frame $\mathcal{F}_p$, with origin on the normal projection of W on the path. Then, the car configuration with respect to the path is defined by x, the Cartesian abscissa of W in $\mathcal{F}_p$, and by θ, the car orientation with respect to the path tangent [(see Fig. 2(b)]. Describing the car motion through the model of a unicycle, with an upper curvature bound $c_M \in \mathbb{R}^+$, x and θ evolve according to

$$\begin{aligned} \dot{x} &= v \sin\theta \\ \dot{\theta} &= \omega \end{aligned} \qquad \left|\frac{\omega}{v}\right| < c_M, \tag{1}$$

where v and ω represent, respectively, the linear and angular velocity of the unicycle. The front wheel orientation ϕ can be approximately related to v and ω through

$$\phi = \arctan\left(\frac{\omega l}{v}\right), \tag{2}$$

with l the constant distance between the rear and front wheel axes.*

Note that a complete car-like model could have been used, for control design purposes, by considering the front wheels orientation derivative as the control input. The unicycle stabilizing controller adopted in this paper can in fact be easily extended to include the dynamics of the front wheels orientation, for example, through backstepping techniques. However, in this case, a feedback

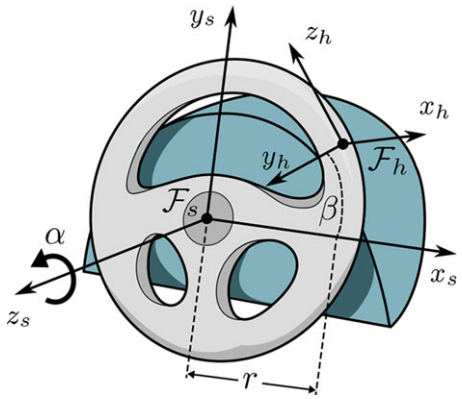

FIGURE 3 The steering wheel, with rotation angle α, hand and steering frames, $\mathcal{F}_h$ and $\mathcal{F}_s$. The parameters r, the radius of the wheel, and β, characterizing the grasp configuration, are also shown here

from wheel orientation would have been required by the controller, but is, generally, not available. A far more practical solution is to neglect the front wheels orientation dynamics, usually faster than that of the car, and consider a static relationship between the front wheels orientation and the car angular velocity. This will only require a rough guess on the value of the parameter l, since the developed controller shows some robustness with respect to model parameters uncertainties as will be shown in Section 5.

The steering wheel is shown in Figure 3, where we indicate, respectively, with $\mathcal{F}_h$ and $\mathcal{F}_s$, the hand and steering wheel reference frames. The origin of $\mathcal{F}_s$ is placed at the center of the wheel, and α is the rotation around its z-axis, that points upward. Thus, positive values of α make the car turn left (i.e., lead to negative ω).

Neglecting the dynamics of the steering mechanism,[30] assuming the front wheels orientation ϕ to be proportional to the steering wheel angle α, controlled by the driver hands, and finally assuming small angles $\omega l/v$ in (2), leads to

$$\alpha = k_\alpha \frac{\omega}{v}, \tag{3}$$

with k_α a negative† scalar, characteristic of the car, accounting also for l.

* Bounds on the front wheels orientation characterizing common service cars induce the maximum curvature constraint in (1).

† Because of the chosen angular conventions.

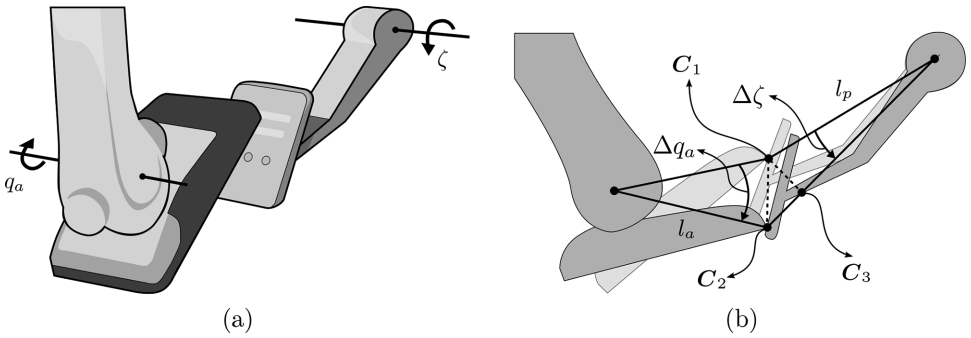

FIGURE 4 (a) The robot foot operates the gas pedal by regulating the joint angle at the ankle q_a, to set a pedal angle ζ, and yield car acceleration a. (b) Geometric relationship between the ankle and the gas pedal angles

The gas pedal is modeled by its inclination angle ζ that yields a given car acceleration $a = dv/dt$. According to experimental observations, at low velocities, the relationship between the pedal inclination and the car acceleration is linear:

$$\zeta = k_\zeta a. \tag{4}$$

The pedal is actuated by the motion of the robot foot, that is pushing it [see Fig. 4(a)]. Assuming small values of Δq_a and $\Delta\zeta$, the point of contact between the foot and the pedal can be considered fixed on both the foot and the pedal, that is, the length of the segment $\overline{C_2C_3}$ in Figure 4(b) can be considered close to zero.* Hence, the relationship between Δq_a and $\Delta\zeta$ is easily found to be

$$\Delta\zeta = \frac{l_a}{l_p}\Delta q_a, \tag{5}$$

where l_a (l_p) is the distance of the ankle (pedal) rotation axis from the contact point of the foot with the pedal.

The robot body reference frame $\mathcal{F}_b$ is placed on the robot chest, with x-axis pointing forward and z-axis upward. Both the accelerations measured by the IMU, and the humanoid tasks, are expressed in this frame. We also indicate with $\mathcal{F}_c$ the robot camera frame (see Fig. 2). Its origin is in the optical center of the camera, with the z-axis coincident with the focal axis. The y-axis points downwards, and the x-axis completes the right-handed frame. $\mathcal{F}_c$ is tilted by an angle γ (taken positive downwards) with respect to the frame $\mathcal{F}_w$, whereas the vector $\boldsymbol{p}_c^w = (x_c^w, y_c^w, z_c^w)^T$ indicates the position vector of the camera frame expressed in the car reference frame.

Now, the driving task can be formulated. It consists of leading the car on the path and aligning it with the path tangent:

$$(x, \theta) \to (0, 0), \tag{6}$$

while driving at a desired velocity:

$$v \to v^*. \tag{7}$$

Task (6) is achieved by the steering control that uses the kinematic model (1) and is realized by the robot hand according to the steering angle α. Concurrently, (7) is achieved by the car velocity control realized by the robot foot that sets a proper angle ζ for the gas pedal. The computation of α and ζ relies on the perception module, that is detailed in the next section.

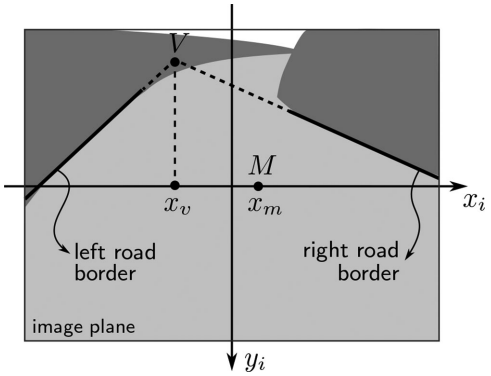

FIGURE 5 The images of the road borders define the middle and vanishing point, respectively, M and V. Their abscissa values are denoted with x_m and x_v

4 | PERCEPTION

The block diagram of Figure 1 shows our perception–action approach. At a higher level, the perception block, whose details are described in this section, provides the feedback signals for the car and robot control.

4.1 | Road detection

This section describes the procedure used to derive the road visual features, required to control the steering wheel.

These visual features are as follows:

(i) the *vanishing point* (V), that is, the intersection of the two borders, and (ii) the *middle point* (M), that is, the midpoint of the segment connecting the intersections of the borders with the image horizontal axis. Both are shown in Figure 5.

Hence, *road detection* consists of extracting the road borders from the robot camera images. After this operation, deriving the vanishing

* For the sake of clarity, in Figure 4(b) the length of the segment $\overline{C_2C_3}$ is much bigger than zero. However, this length, along with angles Δq_a and $\Delta\zeta$, is almost null.

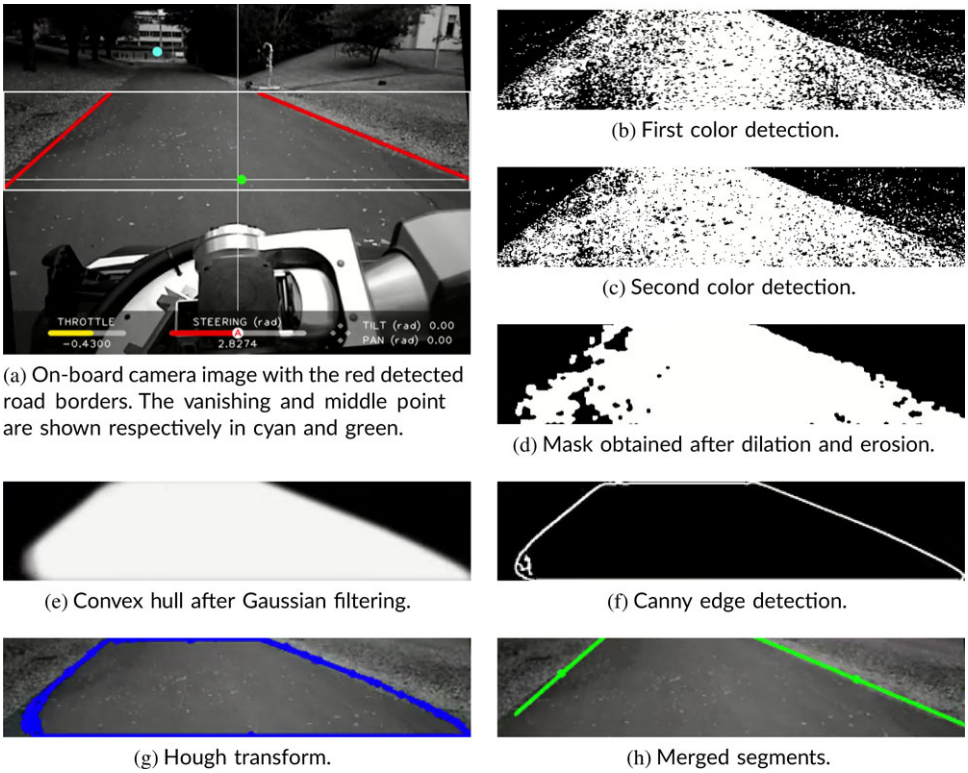

(a) On-board camera image with the red detected road borders. The vanishing and middle point are shown respectively in cyan and green.

(b) First color detection.

(c) Second color detection.

(d) Mask obtained after dilation and erosion.

(e) Convex hull after Gaussian filtering.

(f) Canny edge detection.

(g) Hough transform.

(h) Merged segments.

FIGURE 6 Main steps of the road detection algorithm. Although the acquired robot image (a) is shown in gray scale here, the proposed road detection algorithm processes color images

and middle point is trivial. Since the focus of this work is not to advance the state-of-the-art understanding on road/lane detection, but rather to propose a control architecture for humanoid car driving, we develop a simple image processing algorithm for road border extraction. More complex algorithms can be used to improve the detection and tracking of the road,[31–34] or even to detect road markings.[35] However, our method has the advantage of being based solely on vision, avoiding the complexity induced by integration of other sensors.[36,37] Note that more advanced software is owned by car industries and therefore hard to find in open-code source or binary.

Part of the road borders extraction procedure follows standard techniques used in the field of computer vision[38] and is based on the OpenCV library[39] that provides ready-to-use methods for our vision-based algorithm. More in detail, the steps used for the detection of the road borders on the currently acquired image are described below, with reference to Figure 6.

- From the image, a region of interest (ROI), shown with white borders in Figure 6(a), is manually selected at the initialization and kept constant during the driving experiment. Then, at each cycle of the image processing, we compute the average and standard deviation of hue and saturation channels of the HSV (hue, saturation and value) color space on two central rectangular areas in the ROI. These values are considered for the thresholding operations described in the next step.
- Two binary images [Figs. 6(b) and 6(c)] are obtained by discerning the pixels in the ROI, whose hue and saturation value are in the ranges (average ± standard deviation) defined in the previous step. This operation allows to detect the road, while being adaptive to color variation. The HSV value channel is not considered, to be robust to luminosity changes.
- To remove "salt and pepper noise," the dilation and erosion operators are applied to the binary images. Then, the two images are merged by using the OR logic operator to obtain a mask of the road [Fig. 6(d)].
- The convex hull is computed with areas greater than a given threshold on the mask found in the previous step; then, a Gaussian filter is applied for smoothing. The result is shown in Figure 6(e).
- The Canny edge detector [Fig. 6(f)], followed by Hough transform [Fig. 6(g)], is applied to detect the line segments on the image.
- Similar segments are merged,* as depicted in Figure 6(h).

This procedure gives two lines corresponding to the image projection of the road borders. However, in real working conditions, it may happen that one or both the borders are not detectable because of noise on the image, or failures in the detection process. For this reason, we added a recovery strategy, as well as a tracking procedure, to the pipeline. The recovery strategy consists of substituting the borders, which are not detected, with artificial ones, defined offline as oblique lines that, according to the geometry of the road and to the configuration of the camera, most likely correspond to the road borders. This allows the computation of the vanishing and middle point even when one (or both) real road borders are not correctly detected. On the

* For details on this step, refer to Paolillo et al.[28]

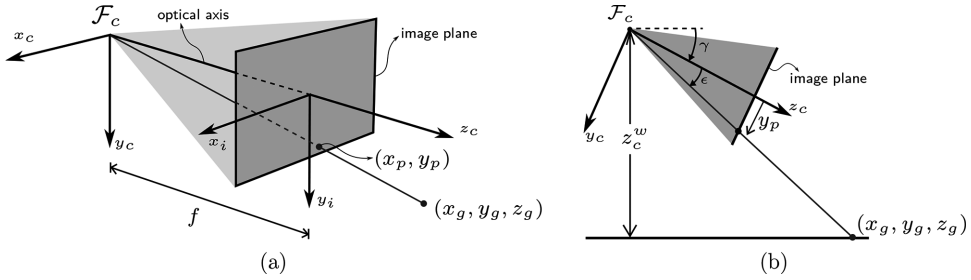

FIGURE 7 Schematic representation of the robot camera looking at the road. (a) Any visible Cartesian point (x_g, y_g, z_g) on the ground has a projection on the camera image plane, whose coordinates expressed in pixels are (x_p, y_p). (b) The measurement of this point on the image plane, together with the camera configuration parameters, can be used to estimate the depth z_g of the point

other hand, the tracking procedure gives continuity and robustness to the detection process, by taking into account the borders detected on the previous image. It consists of a simple KF, with state composed of the slope and intercept of the two borders.* In the prediction step, the KF models the position of lines on the image plane as constant (a reasonable design choice, under Assumption 3, of locally flat and straight road), whereas the measurement step uses the road borders as detected in the current image.

From the obtained road borders (shown in red in Figure 6(a)), the vanishing and middle point are derived, with simple geometrical computations. Their values are then smoothed with a low-pass frequency filter and finally fed to the steering control, which will be described in Section 5.1.

4.2 | Car velocity estimation

To keep the proposed framework independent from the car characteristics, we propose to estimate the car speed v, by using only the robot sensors, and avoiding information coming from the car equipment, such as GPS, or speedometer. To this end, we use the robot camera to measure the optical flow, that is the apparent motion of selected visual features, due to the relative motion between camera and scene.

The literature in the field of autonomous car control provides numerous methods for estimating the car speed by means of optical flow.[40,41] To improve the velocity estimate, the optical flow can be fused with inertial measurements, as done in the case of aerial robots, in Grabe et al.[42] Inspired by that approach, we design a KF, fusing the acceleration measured by the robot IMU and the velocity measured with optical flow.

Considering the linear velocity and acceleration along the forward car axis y_w as state $\boldsymbol{\xi} = (v\ a)^T$ of the KF, we use a simple discrete-time stochastic model to describe the car motion:

$$\boldsymbol{\xi}_{k+1} = \begin{pmatrix} 1 & \Delta T \\ 0 & 1 \end{pmatrix} \boldsymbol{\xi}_k + \boldsymbol{n}_k, \tag{8}$$

with ΔT the sampling time and $\boldsymbol{n}_k$ the zero-mean white Gaussian noise. The corresponding output of the KF is modeled as

$$\boldsymbol{\eta}_k = \boldsymbol{\xi}_k + \boldsymbol{m}_k, \tag{9}$$

* Although three parameters are sufficient if the borders are parallel, a four-dimensional state vector will cover all cases, while guaranteeing robustness to image processing noise.

where $\boldsymbol{m}_k$ indicates the zero-mean white Gaussian noise associated with the measurement process. The state estimate is corrected, thanks to the computation of the residual, that is, the difference between measured and predicted outputs. The measurement is based on both the optical flow (v_{OF}), and the output of the IMU accelerometers (a_{IMU}). Then, the estimation of the car velocity v will correspond to the first element of state vector $\boldsymbol{\xi}$. The process to obtain v_{OF} and a_{IMU} is detailed below.

4.2.1 | Measure of the car speed with optical flow

To measure the car velocity v_{OF} in the KF, we use optical flow. Optical flow can be used to reconstruct the motion of the camera, and from that, assuming that the transformation from the robot camera frame to the car frame is known, it is straightforward to derive the vehicle velocity.

More in detail, the six-dimensional velocity vector $\boldsymbol{v}_c$ of the frame $\mathcal{F}_c$ can be related to the velocity of the point tracked in the image $\dot{\boldsymbol{x}}_p$ through the following relation:

$$\dot{\boldsymbol{x}}_p = \boldsymbol{L}\boldsymbol{v}_c, \tag{10}$$

where the interaction matrix $\boldsymbol{L}$ is expressed as follows[43]:

$$\boldsymbol{L} = \begin{pmatrix} -\frac{S_x}{z_g} & 0 & \frac{x_p}{z_g} & \frac{x_p y_p}{S_y} & -(S_x + \frac{x_p^2}{S_x}) & \frac{y_p S_x}{S_y} \\ 0 & -\frac{S_y}{z_g} & \frac{y_p}{z_g} & S_y + \frac{y_p^2}{S_y} & -\frac{x_p y_p}{S_x} & -\frac{x_p S_y}{S_x} \end{pmatrix}. \tag{11}$$

Here, (x_p, y_p) are the image coordinates (in pixels) of the point on the ground, expressed as (x_g, y_g, z_g) in the camera frame (see Fig. 7). Furthermore, it is $S_{x,y} = f\alpha_{x,y}$, where f is the camera focal length and α_x/α_y the pixel aspect ratio. In the computation of $\boldsymbol{L}$, we consider that the image principal point coincides with the image center. As shown in Figure 7(b), the point depth z_g can be reconstructed through the image point ordinate y_p and the camera configuration (tilt angle γ and height z_c^w):

$$z_g = \frac{z_c^w \cos\epsilon}{\sin(\gamma + \epsilon)}, \quad \epsilon = \arctan\left(\frac{y_p}{S_y}\right). \tag{12}$$

Actually, the camera velocity $\boldsymbol{v}_c$ is computed by taking into account n tracked points, that is, in (10), we consider, respectively, $\hat{\boldsymbol{L}} = (\boldsymbol{L}_1 \cdots \boldsymbol{L}_n)^T$

and $\hat{\dot{\boldsymbol{x}}}_p = (\dot{\boldsymbol{x}}_{p,1} \cdots \dot{\boldsymbol{x}}_{p,n})^T$, instead of $\boldsymbol{L}$ and $\dot{\boldsymbol{x}}_p$. Then, $\boldsymbol{v}_c$ is obtained by solving a least-squares problem*:

$$\boldsymbol{v}_c = \arg\min_{\boldsymbol{\chi}} ||\hat{\boldsymbol{L}}\boldsymbol{\chi} - \hat{\dot{\boldsymbol{x}}}_p||_2. \tag{13}$$

The reconstruction of $\hat{\dot{\boldsymbol{x}}}_p$ in (13) is based on the computation of the optical flow. However, during the navigation of the car, the vibration of the engine, poor textured views, and other unmodeled effects add noise to the measurement process.[40] Furthermore, other factors, such as variable light conditions, shadows, and repetitive textures, can jeopardize feature tracking. Therefore, raw optical flow, as provided by off-the-shelf algorithms, for example, from the OpenCV library,[39] gives noisy data that are insufficient for accurate velocity estimation; so filtering and outlier rejection techniques must be added.

Since the roads are generally poor in features, we use a *dense* optical flow algorithm that differs from *sparse* algorithms, in that it computes the apparent motion of all the pixels of the image plane. Then, we filter the dense optical flow, first according to geometric rationales, and then with an outlier rejection method.[41] The whole procedure is described below, step by step:

- Take two consecutive images from the robot on-board camera.
- Consider only the pixels in a ROI that includes the area of the image plane corresponding to the road. This ROI is kept constant along all the experiment and, thus, identical for the two consecutive frames.
- Covert the frames to gray scale, apply a Gaussian filter, and equalize with respect to the histogram. This operation reduces the measurement noise and robustifies the method with respect to light changes.
- Compute the dense optical flow, using the Farnebäck algorithm[44] implemented in OpenCV.
- Since the car is supposed to move forward, in the dense optical flow vector, consider only those elements pointing downwards on the image plane, and discard those not having a significant centrifugal motion from the principal point. Furthermore, consider only contributions with length between an upper and a lower threshold and whose origin is on an image edge (detected applying Canny operator).
- Reject the outliers, that is, the contributions $(\dot{x}_{p,i}, \dot{y}_{p,i})$, $i \in \{1, \dots, n\}$, such that $\dot{x}_{p,i} \notin [\bar{\dot{x}}_p \pm \sigma_x]$ and $\dot{y}_{p,i} \notin [\bar{\dot{y}}_p \pm \sigma_y]$, where $\bar{\dot{x}}_p$ ($\bar{\dot{y}}_p$) and σ_x (σ_y) are the average and standard deviation of the optical flow horizontal (vertical) contributions. This operation is made separately for the contributions of the right and left side of the image, where the module and the direction of the optical flow vectors can be quite different (e.g., on turns).

The final output of this procedure, $\hat{\dot{\boldsymbol{x}}}_p$, is fed to (13), to obtain $\boldsymbol{v}_c$, that is then low-pass filtered. To transform the velocity $\boldsymbol{v}_c$ in frame $\mathcal{F}_c$, obtained from (13), into velocity $\boldsymbol{v}_w$ in the car frame $\mathcal{F}_w$, we apply:

$$\boldsymbol{v}_w = \boldsymbol{W}_c^w \boldsymbol{v}_c, \tag{14}$$

* To solve the least-square problem, $n \geq 3$ points are necessary. In our implementation, we used the openCV *solve* function, and to filter the noise due to few contributions, we set $n \geq 25$. If $n < 25$, we set $\boldsymbol{v}_c = 0$.

with $\boldsymbol{W}_c^w$ the twist transformation matrix

$$\boldsymbol{W}_c^w = \begin{pmatrix} \boldsymbol{R}_c^w & \boldsymbol{S}_c^w \boldsymbol{R}_c^w \\ \boldsymbol{0}_{3\times 3} & \boldsymbol{R}_c^w \end{pmatrix}, \tag{15}$$

$\boldsymbol{R}_c^w$ is the rotation matrix from car to camera frame and $\boldsymbol{S}_c^w$ is the skew symmetric matrix associated with the position $\boldsymbol{p}_c^w$ of the origin of $\mathcal{F}_c$ in $\mathcal{F}_w$.

Finally, the speed of the car is set as the y-component of $\boldsymbol{v}_w$: $v_{\text{OF}} = v_{w,y}$. This will constitute the first component of the KF measurement vector.

4.2.2 | Measure of the car acceleration with robot accelerometers

The IMU mounted on-board the humanoid robot is used to measure acceleration, to improve the car velocity estimation through the KF. In particular, given the raw accelerometer data, we first compensate the gravity component, with a calibration executed at the beginning of each experiment.† This gives $\boldsymbol{a}_b$, the three-dimensional (3D) robot acceleration, expressed in the robot frame $\mathcal{F}_b$. Then, we transform $\boldsymbol{a}_b$ in the car frame $\mathcal{F}_w$, to obtain

$$\boldsymbol{a}_w = \boldsymbol{R}_b^w \boldsymbol{a}_b, \tag{16}$$

where $\boldsymbol{R}_b^w$ is the rotation matrix relative to the robot body - vehicle transformation. Finally, a_{IMU} is obtained by selecting the y-component of $\boldsymbol{a}_w$. This will constitute the second component of the KF measurement vector.

5 | CAR CONTROL

The objective of car control is (i) to drive the rear wheel axis center W along the curvilinear path that is equally distant from the left and right road borders [see Fig. 2(b)], while aligning the car with the tangent to this path, and (ii) to track desired vehicle velocity v^*. Basically, car control consists of achieving tasks (6) and (7), with the steering and car velocity controllers described in the following subsections.

5.1 | Steering control

Given the visual features extracted from the images of the robot on-board camera, the vision-based steering controller generates the car angular velocity input ω to regulate both x and θ to zero. This reference input is eventually translated in motion commands for the robot hands.

The controller is based on the algorithm introduced by Toibero et al.[45] for unicycle corridor following and recently extended to the navigation of humanoids in environments with corridors connected through curves and T-junctions.[28] In view of Assumption 3 in Section 2, the same algorithm can be applied here. For the sake of completeness, in the following, we briefly recall the derivation of the features model (that can be found, e.g., also in Vassallo et al.[46]) and the control law

† The assumption on horizontal road in Section 3 avoids the need for repeating this calibration.

originally presented by Toibero et al.[45] In doing so, we illustrate the adaptations needed to deal with the specificity of our problem.

The projection matrix transforming the homogeneous coordinates of a point, expressed in $\mathcal{F}_p$, to its homogeneous coordinates in the image, is

$$\boldsymbol{P} = \boldsymbol{K}\,\boldsymbol{T}_w^c\,\boldsymbol{T}_p^w, \tag{17}$$

where $\boldsymbol{K}$ is the camera calibration matrix,[47] $\boldsymbol{T}_w^c$ is the transformation from the car frame $\mathcal{F}_w$ to $\mathcal{F}_c$, and $\boldsymbol{T}_p^w$ is from the path frame $\mathcal{F}_p$ to $\mathcal{F}_w$.

As intuitive from Figure 2, the projection matrix depends on both the car coordinates and the camera intrinsic and extrinsic parameters. Here, we assume that the camera principal point coincides with the image center, and we neglect image distortion. Furthermore, $\boldsymbol{P}$ has been computed neglecting the z-coordinates of the features, since they do not affect the control task. Under these assumptions, using $\boldsymbol{P}$, the abscissas of the vanishing and middle point, respectively, denoted by x_v and x_m, can be expressed as[45,46]:

$$\begin{aligned} x_v &= k_1 \tan\theta \\ x_m &= k_2 \frac{x}{c_\theta} + k_3 \tan\theta + k_4, \end{aligned} \tag{18}$$

where

$$\begin{aligned} k_1 &= -S_x/c_\gamma \\ k_2 &= -S_x s_\gamma / z_c^w \\ k_3 &= -S_x c_\gamma - S_x s_\gamma y_c^w / z_c^w \\ k_4 &= -S_x s_\gamma x_c^w / z_c^w. \end{aligned}$$

We denote $\cos(*)$ and $\sin(*)$ with c_* and s_*, respectively. Note that with respect to the visual features model in Toibero et al.[45] and Vassallo et al.,[46] the expression of the middle point changes, due to the introduction of the lateral and longitudinal displacement, x_c^w and y_c^w, respectively, of the camera frame with respect to the car frame. As a consequence, to regulate the car position to the road center, we must define a new visual feature $\bar{x}_m = x_m - k_4$. Then, the navigation task (6) is equivalent to the following visual task:

$$(\bar{x}_m, x_v) \to (0, 0). \tag{19}$$

In fact, according to (18), asymptotic convergence of x_v and $\bar{x}_m$ to zero implies convergence of x and θ to zero, achieving the desired path following task.

Feedback stabilization of the dynamics of $\bar{x}_m$ is given by the following angular velocity controller[45]:

$$\omega = \frac{k_1}{k_1 k_3 + \bar{x}_m x_v}\left(-\frac{k_2}{k_1} v x_v - k_p \bar{x}_m\right), \tag{20}$$

with k_p a positive scalar gain. This controller guarantees asymptotic convergence of both $\bar{x}_m$ and x_v to zero, under the conditions that $v > 0$, and that k_2 and k_3 have the same sign, which is always true if (i) $\gamma \in (0, \pi/2)$ and (ii) $y_c^w > -z_c^w / \tan\gamma$, two conditions always verified with the proposed setup.

Note that this controller has been obtained considering the assumption of parallel road borders. Nevertheless, this assumption can be easily relaxed since we showed in Paolillo et al.[28] that the presence of nonparallel borders does not jeopardize the controller's local convergence.

To realize the desired ω in (20), the steering wheel must be turned according to (3):

$$\alpha = \frac{k_\alpha k_1}{k_1 k_3 + \bar{x}_m x_v}\left(-\frac{k_2}{k_1} x_v - k_p \frac{\bar{x}_m}{v}\right), \tag{21}$$

where $\bar{x}_m$ and x_v are obtained by the image-processing algorithm of Section 4.1, whereas the value of v is estimated through the velocity estimation module presented in Section 4.2.

5.2 | Car velocity control

In view of the assumption of low acceleration, and by virtue of the linear relationship between the car acceleration and the pedal angle (Eq. (4)) to track a desired car linear velocity v^* we designed a proportional integral derivative (PID) feedback controller to compute the gas pedal command:

$$\zeta = k_{v,p}\, e_v + k_{v,i} \int e_v + k_{v,d} \frac{d}{dt} e_v. \tag{22}$$

Here, $e_v = (v^* - v)$ is the difference between the desired and current value of the velocity, as computed by the car velocity estimation block, whereas $k_{v,p}$, $k_{v,i}$, and $k_{v,d}$ are the positive proportional, integral, and derivative gains, respectively. In the design of the velocity control law, we decided to insert an integral action to compensate for constant disturbances (like, e.g., the effect of a small road slope) at steady state. The derivative term helped achieving a damped control action. The desired velocity v^* is set constant here.

6 | ROBOT CONTROL

This section presents the lower level of our controller, which enables the humanoid robot to turn the driving wheel by α, and push the pedal by ζ.

6.1 | Wheel operation

The reference steering angle α is converted to the reference pose of the hand grasping the wheel, through the rigid transformation

$$\boldsymbol{T}_h^{b*} = \boldsymbol{T}_s^b(\alpha)\,\boldsymbol{T}_h^s(r, \beta).$$

Here, $\boldsymbol{T}_h^{b*}$ and $\boldsymbol{T}_s^b$ are the transformation matrices expressing, respectively, the poses of frames $\mathcal{F}_h$ and $\mathcal{F}_s$ in Figure 3 with respect to $\mathcal{F}_b$ in Figure 2(a). Constant matrix $\boldsymbol{T}_h^s$ expresses the pose of $\mathcal{F}_h$ with respect to $\mathcal{F}_s$ and depends on the steering wheel radius r, and on the angle β parameterizing the hand position on the wheel.

For a safe interaction between the robot hand and the steering wheel, it is obvious to think of an admittance or impedance controller, rather than solely a force or position controller.[48] We choose to use the following admittance scheme:

$$\boldsymbol{f} - \boldsymbol{f}^* = \boldsymbol{M}\Delta\ddot{\boldsymbol{x}} + \boldsymbol{B}\Delta\dot{\boldsymbol{x}} + \boldsymbol{K}\Delta\boldsymbol{x}, \tag{23}$$

where $\boldsymbol{f}$ and $\boldsymbol{f}^*$ are, respectively, the sensed and desired generalized interaction forces in $\mathcal{F}_h$; $\boldsymbol{M}$, $\boldsymbol{B}$, and $\boldsymbol{K} \in \mathbb{R}^{6\times 6}$ are, respectively, the mass, damping, and stiffness diagonal matrices. As a consequence of the

force $\boldsymbol{f}$ applied on $\mathcal{F}_h$, and on the base of the values of the admittance matrices, (23) generates variations of pose $\Delta\boldsymbol{x}$, velocity $\Delta\dot{\boldsymbol{x}}$ and acceleration $\Delta\ddot{\boldsymbol{x}}$ of $\mathcal{F}_h$ with respect to $\mathcal{F}_s$. Thus, the solution of (23) leads to the vector $\Delta\boldsymbol{x}$ that can be used to compute the transformation matrix $\Delta\boldsymbol{T}$ and to build up the new desired pose for the robot hands:

$$\boldsymbol{T}_h^b = \boldsymbol{T}_h^{b*} \cdot \Delta\boldsymbol{T}. \tag{24}$$

In cases where the admittance controller is not necessary, we simply set $\Delta\boldsymbol{T} = \boldsymbol{I}$.

6.2 | Pedal operation

Since there exists a linear relationship between the variation of the robot ankle and the variation of the gas pedal angle, to operate the gas pedal it is sufficient to move the ankle joint angle q_a. From (22), we compute the command for the robot ankle's angle as

$$q_a = \frac{\zeta}{\zeta_{\max}}(q_{a,\max} - q_{a,\min}) + q_{a,\min}. \tag{25}$$

Here, $q_{a,\max}$ is the robot ankle configuration, at which the foot pushes the gas pedal, producing a significant car acceleration. Instead, at $q_a = q_{a,\min}$, the foot is in contact with the pedal, but not yet pushing it. These values depend both on the car type and on the position of the foot with respect to the gas pedal. A calibration procedure is run before starting driving, to identify the proper values of $q_{a,\min}$ and $q_{a,\max}$. Finally, $\zeta_{\max}$ is set to avoid large accelerations, while saturating the control action.

6.3 | Humanoid task-based control

As shown above, wheel and pedal operation are realized, respectively, in the operational space (by defining a desired hand pose $\boldsymbol{T}_h^b$) and in the articular space (via the desired ankle joint angle q_a). Both can be realized using our task-based QP controller, assessed in complex tasks such as ladder climbing.[49] The joint angles and desired hand pose are formulated as errors that appear among the sum of weighted least-squares terms in the QP cost function. Other intrinsic robot constraints are formulated as linear expressions of the QP variables and appear in the constraints. The QP controller is solved at each control step. The QP variable vector $\boldsymbol{x} = (\ddot{\boldsymbol{q}}^T, \lambda^T)^T$ gathers the joint acceleration $\ddot{\boldsymbol{q}}$, and the linearized friction cones' base weights λ, such that the contact forces $\boldsymbol{f}$ are equal to $\boldsymbol{K}_f\lambda$ (with $\boldsymbol{K}_f$ the discretized friction cone matrix). The desired acceleration $\ddot{\boldsymbol{q}}$ is integrated twice to feed the low-level built-in PD control of HRP-2Kai. The driving task with the QP controller is written as follows:

$$\begin{aligned}
&\underset{\boldsymbol{x}}{\text{minimize}} \sum_{i=1}^{N} w_i \|\boldsymbol{E}_i(\boldsymbol{q}, \dot{\boldsymbol{q}}, \ddot{\boldsymbol{q}})\|^2 + w_\lambda \|\lambda\|^2 \\
&\text{subject to} \\
&(1)\ \text{dynamic constraints} \\
&(2)\ \text{sustained contact positions} \\
&(3)\ \text{joint limits} \\
&(4)\ \text{nondesired collision avoidance constraints} \\
&(5)\ \text{self-collision avoidance constraints,}
\end{aligned} \tag{26}$$

TABLE 2 QP weights and set-point gains

	$\boldsymbol{E}_1$	$\boldsymbol{E}_2$	$\boldsymbol{E}_3$	$\boldsymbol{E}_4$
w	100	5	1000	1000
K_p	5	1 (ankle = 100)	10	10

where w_i and w_λ are task weights or gains and $\boldsymbol{E}_i(\boldsymbol{q}, \dot{\boldsymbol{q}}, \ddot{\boldsymbol{q}})$ is the error in the task space. Details on the QP constraints (since they are common to most tasks) can be found in Vaillant et al.[49]

Here, we explicit the tasks used specifically during the driving (i.e., after the driving posture is reached). We use four ($N = 4$) set-point objective tasks; Each task (i) is defined by its associated task-error $\boldsymbol{\epsilon}_i$ so that $\boldsymbol{E}_i = K_{p_i}\boldsymbol{\epsilon}_i + K_{v_i}\dot{\boldsymbol{\epsilon}}_i + \ddot{\boldsymbol{\epsilon}}_i$.

The driving wheel of the car has been modeled as another "robot" having one joint (rotation). We then merged the model of the driving wheel to that of the humanoid and linked them, through a position and orientation constraint, so that the desired driving wheel steering angle α, as computed by (24), induces a motion on the robot (right arm) gripper. The task linking the humanoid robot to the driving wheel "robot" is set as part of the QP constraints, along with all sustained contacts (e.g., buttock on the car seat, thighs, left foot).

The steering angle α (i.e., the posture of the driving wheel robot) is a set-point task ($\boldsymbol{E}_1$). The robot whole-body posture including the right ankle joint control (pedal) is also a set-point task ($\boldsymbol{E}_2$), which realizes the angle q_a provided by (25). Additional tasks were set to keep the gaze direction constant ($\boldsymbol{E}_3$), and to fix the left arm, to avoid collisions with the car cockpit during the driving operation ($\boldsymbol{E}_4$).

7 | EXPERIMENTAL RESULTS

We tested our driving framework with the full-size humanoid robot HRP-2Kai built by Kawada Industries. For the experiments, we used the Polaris Ranger XP900, the same utility vehicle employed at the DRC. HRP-2Kai has 32 degrees of freedom, is 1.71 m tall and weighs 65 kg. It is equipped with an Asus Xtion Pro 3D sensor, mounted on its head and used in this work as a monocular camera. The Xtion camera provides images at 30 Hz with a resolution of 640×480 pixels. From camera calibration, it results $S_x \simeq S_y = 535$ pixels. In the presented experiments, $x_c^w = -0.4$ m, $y_c^w = 1$ m and $z_c^w = 1.5$ m were manually measured. However, it would be possible to estimate the robot camera position, with respect to the car frame, by localization of the humanoid[50] or by using the geometric information of the car (that can be known, e.g., in the form of a CAD model, as shown in Fig. 2). HRP-2Kai is also equipped with an IMU (of rate 500 Hz) located in the chest. Accelerometer data have been merged with the optical flow to estimate the car linear velocity, as explained in Section 4.2. Furthermore, a built-in filter processes the IMU data to provide an accurate measurement of the robot chest orientation. This is kinematically propagated up to the Xtion sensor to get γ, the tilt angle of the camera with respect to the ground.

The task-based control is realized through the QP framework (see Section 6.3) which allows to easily set different tasks that can be achieved concurrently by the robot. Table2 gives the weights

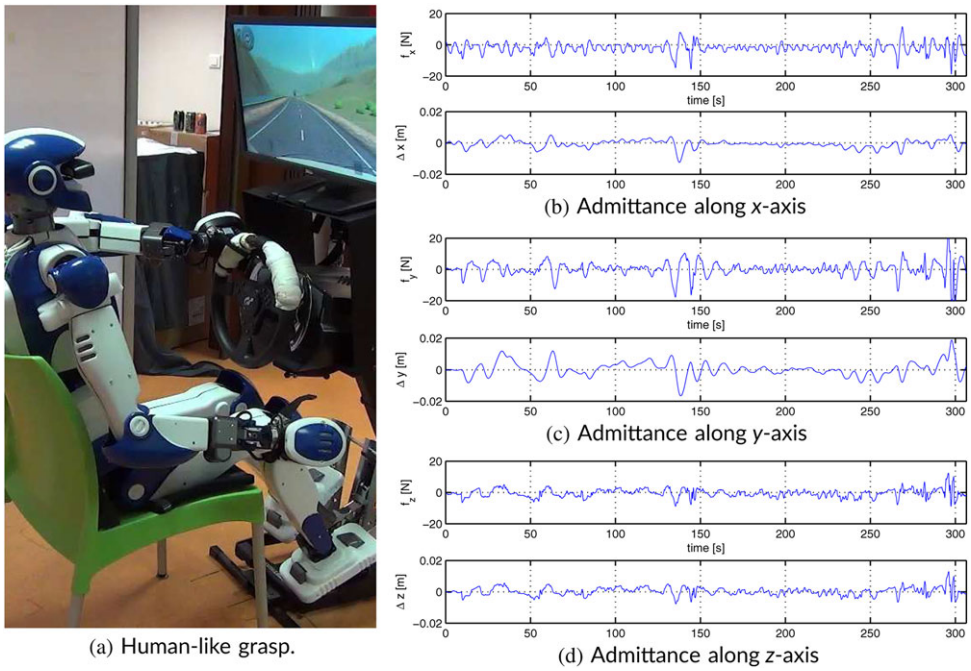

FIGURE 8 Left: Setup of an experiment that requires admittance control on the steering hand. Right: Output of the admittance controller in the hand frame during the same experiment

of the four set-point tasks described in Section 6.3. Note that $K_{v_i} = 2 \times \sqrt{K_{p_i}}$.

As for the gains in Section 5, we set $k_{v,p} = 10^{-8}$, $k_{v,d} = 3 \times 10^{-9}$ and $k_{v,i} = 2 \times 10^{-9}$ to track the car desired velocity v^*, whereas in the steering wheel controller we choose the gain $k_p = 3$, and we set the parameter $k_\alpha = -5$. While the controller gains have been chosen as a trade-off between reactivity and control effort, the parameter k_α was roughly estimated. Given the considered scenario, an exact knowledge of this parameter is generally not possible, since it depends on the car characteristics. It is however possible to show that, at the kinematic level, this kind of parameter uncertainty will induce a nonpersistent perturbation on the nominal closed loop dynamics.

Proving the boundedness of the perturbation term induced by parameter uncertainties would allow to conclude about the local asymptotic stability of the perturbed system. In general, this would imply a bound on the parameter uncertainty to be satisfied to preserve local stability. While this analysis is beyond the scope of this paper, we also note that in practice it is not possible to limit the parameter uncertainty that depends on the car and the environment characteristics. Therefore, we rely on the experimental verification of the vision-based controller robustness, delegating to the framework modes (autonomous, shared-autonomy, or teleoperated) the task of taking the controller within its region of local asymptotic stability. In other words, when the system is too far from the equilibrium condition and convergence of the vision-based controller could be compromised, due to model uncertainties and unexpected perturbations, the user can always resort to the other driving modes.

In the KF used for the car velocity estimation, the process and the measurement noise covariance matrices are set to diag($1e^{-4}$, $1e^{-4}$) and diag($1e^2$, $1e^2$), respectively. Since the forward axis of the robot frame is aligned with the forward axis of the vehicle frame, to get a_{IMU} we did not apply the transformation (16), but we simply collected the acceleration along the forward axis of the robot frame, as given by the accelerometers. The sampling time of the KF was set to $\Delta T = 0.002$ s (being 500 Hz the frequency of the IMU measurements, the filter runs at the same rate).

The cutoff frequencies of the low-pass filters were applied to the visual features, and the car velocity estimate were set to 8 and 2.5 Hz, respectively.

At the beginning of each campaign of experiments, we arrange the robot in the correct driving posture in the car as shown in Figure 9(a). This posture (except for the driving leg and arm) is assumed constant during driving: All control parameters are kept constant. At initialization, we also correct eventual bad orientations of the camera with respect to the ground plane, by applying a rotation to the acquired image, and by regulating the pitch and yaw angles of the robot neck, so as to align the focal axis with the forward axis of the car reference frame. The right foot is positioned on the gas pedal, and the calibration procedure described in Section 6.2 is used to obtain $q_{a,\max}$ and $q_{a,\min}$.

To ease full and stable grasping of the steering wheel, we designed a handle, fixed to the wheel [visible in Fig. 9(a)], allowing the alignment of the wrist axis with that of the steer. With reference to Figure 3, this corresponds to configuring the hand grasp with $r = 0$ and, to comply with the shape of the steering wheel, $\beta = 0.57$ rad. Owing to the robot kinematic constraints, such as joint limits and autocollisions avoidance, imposed by our driving configuration, the range of the steering angle α is restricted from approximately −2 to −3 rad. These limits cause bounds on the maximum curvature realizable by the car. Nevertheless, all of the followed paths were compatible with this constraint. For more challenging maneuvers, grasp reconfiguration should be integrated in the framework.

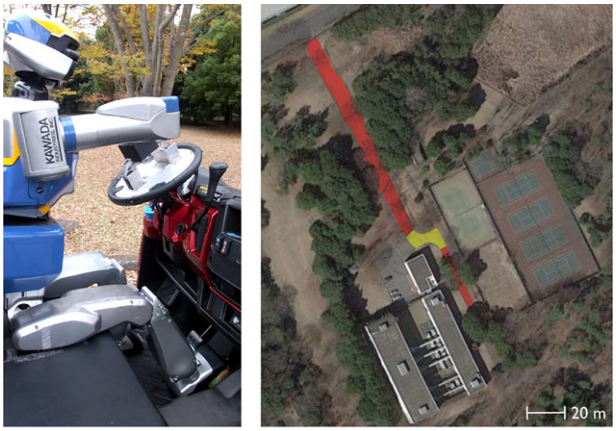

(a) Driving posture (b) Top view of the experimental area

FIGURE 9 The posture taken by HRP-2Kai during the experiments (a) and the experimental area at the National Institute of advanced industrial science and technology (AIST) campus (b)

With this grasping setup, we achieved a good alignment between the robot hand and the steering wheel. Hence, during driving, the robot did not violate the geometrical constraints imposed by the steering wheel mechanism. In this case, the use of the admittance control for safe manipulation is not necessary. However, we showed in Paolillo et al.[15] that the admittance control can be easily plugged in our framework, whenever needed. In fact, in that work, an HRP-4, from Kawada Industries, turns the steering wheel with a more "human-like" grasp [$r = 0.2$ m and $\beta = 1.05$ rad; see Fig. 8(a)]. Owing to the characteristics of both the grasp and the HRP-4 hand, admittance control is necessary. For sake of completeness, we report in Figures 8(b)–8(d) plots of the admittance behavior relative to that experiment. In particular, to have good tracking of the steering angle α, while complying with the steering wheel geometric constraint, we designed a fast (stiff) behavior along the z-axis of the hand frame, $\mathcal{F}_h$ and a slow (compliant) along the x- and y-axes. To this end, we set the admittance parameters: $m_x = m_y = 2000$ kg, $m_z = 10$ kg, $b_x = b_y = 1600$ kg/s, $b_z = 240$ kg/s, and $k_x = k_y = 20$ kg/s^2, $k_z = 1000$ kg/s^2. Furthermore, we set the desired forces $f_x^* = f_z^* = 0$ N, while along the y-axis of the hand frame $f_y^* = 5$ N, to improve the grasping stability. Note that the evolution of the displacements along the x- and y-axes [plots in Figs. 8(b)–8(c)] is the results of a dynamic behavior that filters the high frequency of the input forces, whereas along the z-axis the response of the system is more reactive.

In the rest of this section, we present the HRP-2Kai outdoor driving experiments. In particular, we present the results of the experiments performed at the authorized portion of the AIST campus in Tsukuba, Japan. A top view of this experimental field is shown in Figure 9(b). The areas highlighted in red and yellow correspond to the paths driven using the autonomous and teleoperated mode, respectively, as further described below. Furthermore, we present an experiment performed at the DRC final, showing the effectiveness of the shared-autonomy driving mode. For a quantitative evaluation of the approach, we present the plots of the variables of interest. The same experiments are shown in the video available at https://youtu.be/SYHI2JmJ-Ik that also allows a qualitative evaluation of the online image processing. Quantitatively, we successfully carried out 14 experiments over of 15 repetitions, executed at different times, between 10:30 a.m. and 4 p.m., proving image-processing robustness in different days and time (i.e., under different light conditions).

7.1 | First experiment: autonomous car driving

In the first experiment, we tested the autonomous mode, that is, the effectiveness of our framework to make a humanoid robot drive a car autonomously. For this experiment, we choose $v^* = 1.2$ m/s, whereas the foot calibration procedure gave $q_{a,\max} = -0.44$ rad and $q_{a,\min} = -0.5$ rad.

Figure 10 shows eight snapshots taken from the video of the experiment. The car starts with an initial lateral offset, that is corrected after a few meters. The snapshots (as well as the video) of the experiment show that the car correctly travels at the center of a curved path, for about 100 m. Furthermore, one can observe that the differences in the light conditions (due to the tree shadows) and in the color of the road do not jeopardize the correct detection of the borders and, consequently, the driving performance.

Figure 11 shows the plots related to the estimation of the car speed, as described in Section 4.2. On the top, we plot a_{IMU}, the acceleration along the forward axis of the car, as reconstructed from the robot accelerometers. The center plot shows the car speed measured with the optical flow-based method (v_{OF}), whereas the bottom plot gives the trace of the car speed v obtained by fusing a_{IMU} and v_{OF}. Note that the KF reduces the noise of the v_{OF} signal, a very important feature for keeping the derivative action in the velocity control law (22).

As well known, reconstruction from vision (e.g., the "structure from motion" problem) suffers from a scale problem, in the translation vector estimate.[47] This issue, due to the loss of information in mapping two-dimensional to 3D data, is also present in optical flow velocity estimation methods. Here, this can lead to a scaled estimate of the car velocity. For this reason, we decided to include another sensor information in the estimation process: the acceleration provided by the IMU. Note, however, that in the current state of the work, the velocity estimate accuracy has been only evaluated qualitatively. In fact, that high accuracy is only important in the transient phases (initial error recovery and curve negotiation). Instead, it can be easily shown that the perturbation induced by velocity estimate inaccuracy on the features dynamics vanishes at the regulation point corresponding to the desired driving task, and that by limiting the uncertainty on the velocity value, it is possible to preserve local stability. In fact, the driving performance showed that the estimation was accurate enough, for the considered scenario. In different conditions, finer tuning of the velocity estimator may be necessary.

Plots related to the steering wheel control are shown in Figure 12(a). The steering control is activated about 8 s after the start of the experiment and, after a transient time of a few seconds, it leads the car to the road center. Thus, the middle and vanishing points (the top and center plots, respectively) correctly converge to the desired values, that is, x_m goes to $k_4 = 30$ pixels (since $\gamma = 0.2145$ rad; see expression of k_4 in Section 5.1) and x_v to 0. The bottom plot shows the trend of the desired steering command α, as computed from the visual features and from the estimated car speed according to (21).

FIGURE 10 First experiment: autonomous car driving

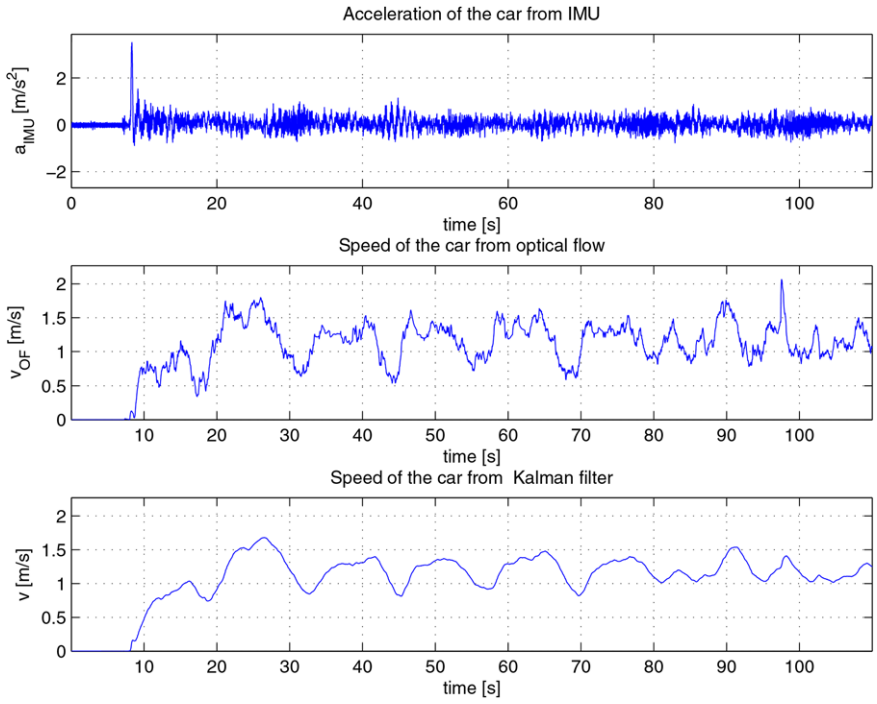

FIGURE 11 First experiment: autonomous car driving. Acceleration a_{IMU} measured with the robot IMU (top), linear velocity v_{OF} measured with the optical flow (center), and car speed v estimated by the KF (bottom)

The same signal, reconstructed from the encoders (black dashed line), shows that the steering command is smoothed by the task-based QP control, avoiding undesirable fast signal variations.

Figure 12(b) presents the plots of the estimated versus desired car speed (top) and the ankle angle command sent to the robot to operate the gas pedal and drive the car at the desired velocity (bottom).

Also in this case, after the initial transient, the car speed converges to the nominal desired values (no ground truth was available). The oscillations observable at steady state are due to the fact that the resolution of the ankle joint is coarser than that of the gas pedal. Note, in fact, that even if the robot ankle moves in a small range, the car speed changes significantly. The noise on the ankle command, as well as the initial peak, are due to the derivative term of the gas pedal control (22). However, the signal is smoothed by the task-based QP control (see the dashed black line, i.e., the signal reconstructed by encoder readings), preventing jerky motion of the robot foot.

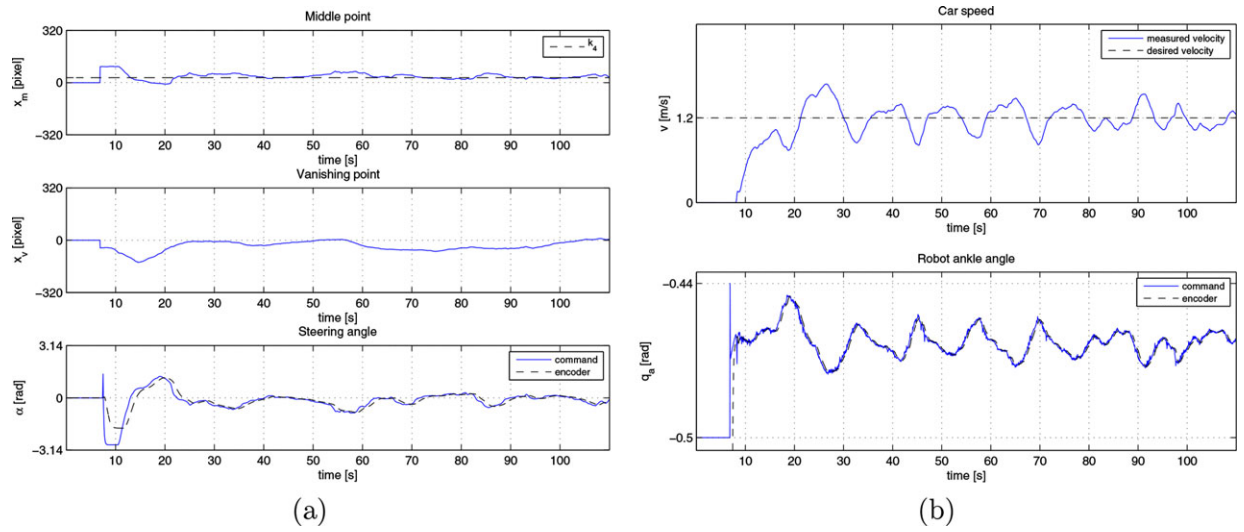

FIGURE 12 First experiment: autonomous car driving. (a) Middle point abscissa x_m (top), vanishing point abscissa x_v (center), and steering angle α (bottom). (b) Car speed v (top), already shown in Figure 10 and ankle joint angle q_a (bottom)

In the same campaign of experiments, we performed 10 autonomous car-driving experiments. In nine of them (including the one presented just above), the robot successfully drove the car for the entire path. One of the experiments failed due to a critical failure of the image processing. It was not possible to perform experiments on other tracks (with different road shapes and environmental conditions), because our application was rejected after complex administrative paperwork required to access other roads in the campus.

7.2 | Second experiment: switching between teleoperated and autonomous modes

In some cases, the conditions ensuring the correct behavior of the autonomous mode are risky. Thus, it is important to allow a user to supervise the driving operation and control the car if required. As described in Section 2, our framework allows a human user to intervene at any time, during the driving operation, to select a particular driving strategy. The second experiment shows the switching between the autonomous and teleoperated modes. In particular, in some phases of the experiment, the human takes control of the robot, by selecting the teleoperated mode. In these phases, proper commands are sent to the robot, to drive the car along two very sharp curves, connecting two straight roads traveled in autonomous mode. Snapshots of this second experiment are shown in Figure 13.

For this experiment, we set $v^* = 1.5$ m/s, while after the initial calibration of the gas pedal, $q_{a,\min} = -0.5$ rad and $q_{a,\max} = -0.43$ rad. Note that the difference in the admissible ankle range with respect to the previous experiment is due to a slightly different position of the robot foot on the gas pedal.

Figure 14(a) shows the signals of interest for the steering control. In particular, one can observe that when the control is enabled (shadowed areas of the plots) there is the same correct behavior of the system seen in the first experiment. When the user asks for the teleoperated mode (nonshadowed areas of the plots), the visual features are not considered and the steering command is sent to the robot via keyboard or joystick by the user. Between 75 and 100 s, the user controlled the robot (in teleoperated mode) to make it steer on the right as much as possible. Because of the kinematic limits and of the grasping configuration, the robot saturated the steering angle at about −2 rad even if the user asked a wider steering. This is evident on the plot of the steering angle command of Figure 14(a) (bottom): note the difference between the command (blue continuous curve) and the steering angle reconstructed from the encoders (black dashed curve).

Similarly, Figure 14(b) shows the gas pedal control behavior when switching between the two modes. When the gas pedal control is enabled, the desired car speed is properly tracked by operating the robot ankle joint [shadowed areas of the top plot in Fig. 14(b)]. On the other hand, when the control is disabled (nonshadowed areas of the plots), the ankle command [blue curve in Fig. 14(b), bottom], as computed by (25), is not considered, and the robot ankle is teleoperated with the keyboard/joystick interface, as noticeable from the encoder plot (black dashed curve).

At the switching between the two modes, the control keeps sending commands to the robot without any interruption, and the smoothness of the signals allows to have continuous robot operation. In summary, the robot could perform the entire experiment (along a path of 130 m ca. for more than 160 s) without the need to stop the car. This was achieved thanks to two main design choices. First, from a perception viewpoint, monocular camera and IMU data are light to be processed, allowing a fast and reactive behavior. Second, the control framework at all the stages (from the higher level visual control to the low-level kinematic control) guarantees smooth signals, even at the switching moments.

The same experiment presented just above was performed five other times, during the same day. Four experiments resulted successful, whereas two failed due to human errors during teleoperation.

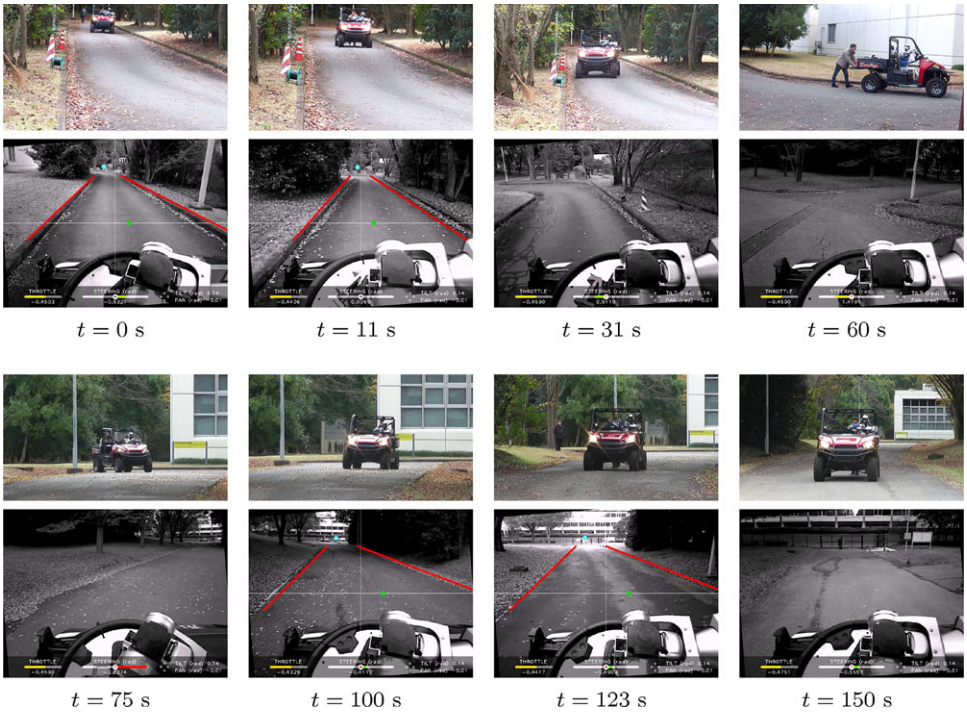

FIGURE 13 Second experiment: switching between teleoperated and autonomous modes

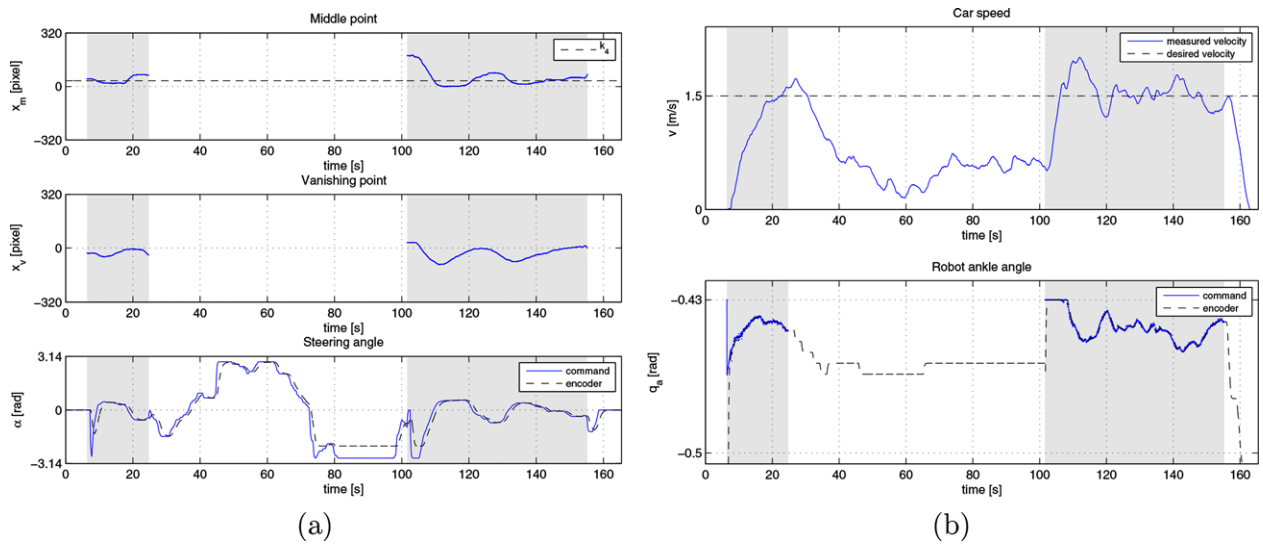

FIGURE 14 Second experiment: switching between teleoperated and autonomous modes. (a) Middle point abscissa x_m (top), vanishing point abscissa x_v (center), and steering angle α (bottom). (b) Car speed v (top) and ankle joint angle q_a (bottom)

7.3 | Third experiment: shared-autonomy driving at the DRC finals

There are situations in which the application of the autonomous mode is too risky (e.g., because of bad quality images) and the full teleoperation mode is too stressful for the operator who must operate continuously along all the experiment a joystick or a keyboard. In these cases, it is convenient to provide the user with the shared-autonomy mode described in Section 2 to help with the steering operations.

This experiment shows the effectiveness of such shared-autonomy mode. This strategy was very useful to make the robot drive at the DRC finals. The challenge presented a lot of uncertainties since the track was not a regular road, but a dirt track marked with Jersey barriers. Furthermore, we had to comply with the competition rules regarding the execution time and the safety of the task execution. For these reasons, we used shared-autonomy that allows defining high target objectives while the steering commands are left to the humanoid robot controller. This frees the user from having to continuously teleoperate the robot. We successfully completed the task on both DRC days (in 1:28 and 1:32 minutes) by using the shared-autonomy mode. Snapshots taken from the DRC finals official video[51] are shown in Figure 15 (they refer to the second day of the competition). The human user teleoperated HRP-2Kai remotely, by using the video stream from the robot camera as the only feedback from the challenge field. In the received

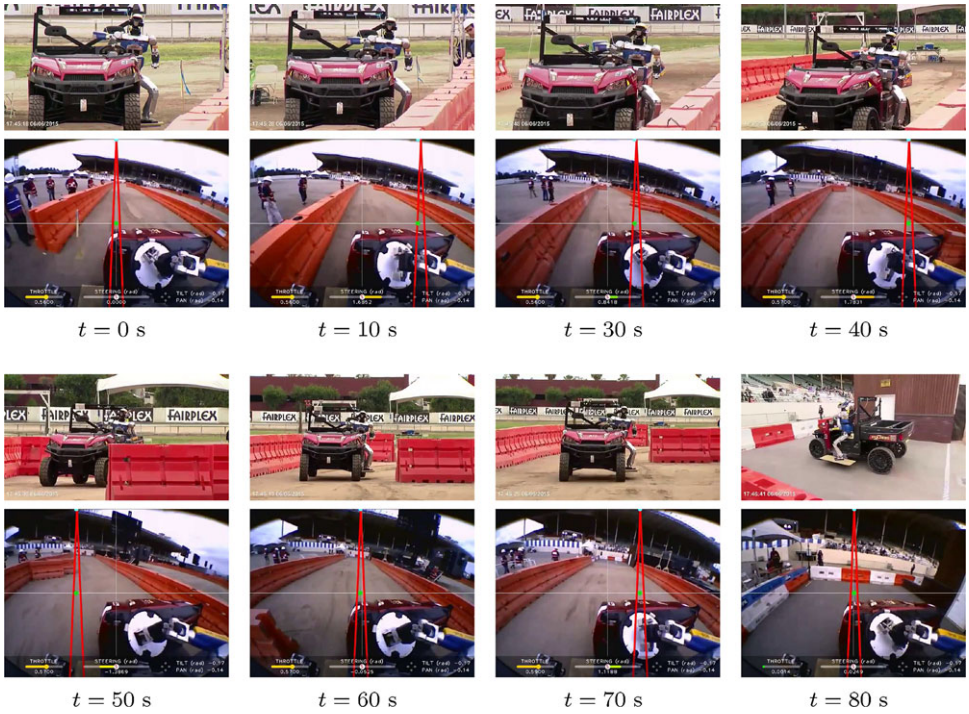

FIGURE 15 Third experiment: shared-autonomy driving mode at the DRC finals. Snapshots taken from the DRC official video

images, the user selected, via mouse, the proper artificial road borders (red lines in the figure) to steer the car along the path. Note that these artificial road borders, manually set by the user, may not correspond to the real borders of the road. In fact, they just represent geometrical references—more intuitive for humans—to easily define the vanishing and middle points and steer the car using (21). Concurrently, the robot ankle was teleoperated to achieve a desired car velocity. In other words, with reference to the block diagram of Figure 1, the user provides the visual features to the steering control and the gas pedal reference to the pedal operation block. Basically, s/he takes the place of the road detection and car velocity estimation/control blocks. The shared-autonomy mode can be seen as a sort of shared control between the robot and the a human supervisor and allows the human to interfere with the robot operation if required. Only one person is required to operate in shared-autonomy or teleoperation modes. Furthermore, in the DRC experiment, the user had to intervene only 15 times along all the experiment to specify the steering commands to the algorithm. This results in a more comfortable steering experience (with respect to the teleoperation mode). As stated in the previous section, at any time, during the execution of the driving experience, the user can instantly and smoothly switch to one of the other two driving modes. At the DRC, we used a wide angle camera, although the effectiveness of the shared-autonomy mode was also verified with a Xtion camera.

8 | CONCLUSIONS

In this paper, we have proposed a reactive control architecture for car driving by a humanoid robot on unknown roads. The proposed approach consists of extracting road visual features to determine a reference steering angle to keep the car at the center of a road. The gas pedal, operated by the robot foot, is controlled by estimating the car speed using visual and inertial data. Three different driving modes (autonomous, shared-autonomy, and teleoperated) extend the versatility of our framework. The experimental results carried out with the humanoid robot HRP-2Kai have shown the effectiveness of the proposed approach. The shared-autonomy mode was successfully used to complete the driving task at the DRC finals.

The driving task was addressed as an explicative case study of humanoids controlling human-tailored devices. In fact, besides the achievement of the driving experience, we believe that humanoids are the most sensible platforms for helping humans with everyday task, and the proposed work shows that complex real-world tasks can be actually performed in autonomous, shared-autonomy, and teleoperated way. Obviously, the complexity of the task comes also with the complexity of the framework design, on both perception and control point of views. This led us to make some working assumptions that, in some cases, limited the range of application of our methods.

Further investigations shall deal with the task complexity to advance the state-of-art knowledge of algorithms and make humanoids capable of helping humans with dirty, dangerous, and demanding jobs. Future work will be done to make the autonomous mode work efficiently in the presence of sharp curves. To this end and to overcome the problem of limited steering motions, we plan to include, in the framework, the planning of variable grasping configurations to achieve more complex maneuvers. We are also planning to go to driving on uneven terrains, where the robot has also to sustain its attitude, with respect to sharp changes of the car orientation. Furthermore, the introduction of obstacle avoidance algorithms,

based on optical flow, will improve the driving safety. Finally, we plan to add brake control and to perform the entire driving task, including car ingress and egress.

ACKNOWLEDGMENTS

This work is supported by the EU FP7 strep project KOROIBOT http://www.koroibot.eu, and by the Japan Society for Promotion of Science (JSPS) Grant-in-Aid for Scientific Research (B) No. 16H02886. This work was also in part supported by the CNRS PICS Project ViNCI.

The authors deeply thank Dr. Eiichi Yoshida for taking in charge the administrative procedures in terms of AIST clearance and transportation logistics, without which the experiments could not be conducted; Dr. Fumio Kanehiro for lending the car and promoting this research; Hervé Audren and Arnaud Tanguy for their kind support during the experiments.

REFERENCES

1. DARPA Robotics Challenge. DRC Finals. http://archive.darpa.mil/roboticschallenge/. Published 2015.
2. Nunes U, Laugier C, Trivedi MM. Guest editorial introducing perception, planning, and navigation for intelligent vehicles. *IEEE Trans Intell Trans Syst*. 2009;10(3):375–379.
3. Zhang Y, Lin W, Chin Y-K. Driving skill characterization: A feasibility study. In: *IEEE International Conference on Robotics and Automation, 2008*. 2008:2571–2576.
4. Hentschel M, Wagner B. Autonomous robot navigation based on open street map geodata. In: *13th International IEEE Conference on Intelligent Transportation Systems*. 2010:1645–1650.
5. Newman P, Sibley G, Smith M, et al. Navigating, recognizing and describing urban spaces with vision and lasers. *Int J Robot Res*. 2009;28(11-12):1406–1433.
6. Broggi A, Bombini L, Cattani S, Cerri P, Fedriga RI. Sensing requirements for a 13,000 km intercontinental autonomous drive. In: *2010 IEEE Intelligent Vehicles Symposium (IV)*. 2010:500–505.
7. Cherubini A, Spindler F, Chaumette F. Autonomous visual navigation and laser-based moving obstacle avoidance. *IEEE Trans Intell Transp Sys*. 2014;31(1–2):2101–2110.
8. Buehler M, Lagnemma K, Singh SE. Special issue on the 2007 DARPA urban challenge, part I–III. *J Field Robot*. 2008;25(8–10):423–860.
9. Thrun S, Montemerlo M, Dahlkamp H, et al. Stanley: the robot that won the DARPA grand challenge. *J Field Robot*. 2006;23(9):661–692.
10. Google. Google self-driving car project. Published 2016. https://waymo.com.
11. Pratt G, Manzo J. The DARPA robotics challenges. *IEEE Robot Autom Mag*. 2013;20(2):10–12.
12. Hasunuma H, Nakashima K, Kobayashi M, et al. A tele-operated humanoid robot drives a backhoe. In: *IEEE International Conference on Robotics and Automation*. 2003:2998–3004.
13. Yokoi K, Nakashima K, et al. A tele-operated humanoid operator. *Int J Robot Res*. 2006;5-6:593–602.
14. Hirata N, Mizutani N, Matsui H, Yano K, Takahashi T. Fuel consumption in a driving test cycle by robotic driver considering system dynamics. In: *2015 IEEE International Conference on Robotics and Automation*. 2015:3374–3379.
15. Paolillo A, Cherubini A, Keith F, Kheddar A, Vendittelli M. Toward autonomous car driving by a humanoid robot: A sensor-based framework. In: *2014 14th IEEE-RAS International Conference on Humanoid Robots*. 2014:451–456.
16. DRC Teams. What happened at the DARPA Robotics Challenge? Published 2015. http://www.cs.cmu.edu/cga/drc/events.
17. Kim S, Kim M, Lee J, et al. Team SNU's control strategies for enhancing a robot's capability: lessons from the 2015 DARPA robotics challenge finals. *J Field Rob*. 2017;34(2):359–380.
18. McGill S, Yi S-J, Lee DD. Team THOR's adaptive autonomy for disaster response humanoids. In: *2015 15th IEEE-RAS International Conference on Humanoid Robots*. 2015:453–460.
19. Johnson M, Shrewsbury B, Bertrand S, et al. Team IHMC's lessons learned from the DARPA robotics challenge: finding data in the rubble. *J Field Robot*. 2017;34(2):241–261.
20. Schwarz M, Rodehutskors T, Droeschel D, et al. NimbRo rescue: solving disaster-response tasks with the mobile manipulation robot Momaro. *J Field Robot*. 2017;34(2):400–425.
21. Haynes GC, Stager D, Stentz A, et al. Developing a robust disaster response robot: CHIMP and the robotics challenge. 2017;34(2):281–304.
22. Marion P, Fallon M, Deits R, et al. Director: a user interface designed for robot operation with shared autonomy. *J Field Robot*. 2017;34(2):262–280.
23. Karumanchi S, Edelberg K, Baldwin I, et al. Team RoboSimian: semi-autonomous mobile manipulation at the 2015 DARPA robotics challenge finals. *J Field Robot*. 2017;34(2):305–332.
24. DeDonato M, Polido F, Knoedler K, et al. Team WPI-CMU: Achieving reliable humanoid behavior in the DARPA robotics challenge. *J Field Robot*. 2017;34(2):381–399.
25. Kumagai I, Terasawa R, Noda S, et al. Achievement of recognition guided teleoperation driving system for humanoid robots with vehicle path estimation. In *2015 15th IEEE-RAS International Conference on Humanoid Robots*. 2015:670–675.
26. Jeong H, Oh J, Kim M, Joo K, Kweon IS, Oh JH. Control strategies for a humanoid robot to drive and then egress a utility vehicle for remote approach. In: *2015 15th IEEE-RAS Int. Conf. on Humanoid Robots*. 2015:811–816.
27. Rasmussen C, Sohn K, Wang Q, Oh P. Perception and control strategies for driving utility vehicles with a humanoid robot. In: *2014 IEEE/RSJ International Conference on Intelligent Robots and Systems*. 2014:973–980.
28. Paolillo A, Faragasso A, Oriolo G, Vendittelli M. Vision-based maze navigation for humanoid robots. *Autonom Robot*. 2016;41(2):1–17. https://doi.org/10.1007/s10514-015-9533-1.
29. De Luca A, Oriolo G. Modelling and control of nonholonomic mechanical systems. In: *Kinematics and Dynamics of Multi-Body Systems, CISM Courses and Lectures, volume 360*. Wien: Springer-Verlag; 1995:277–3429.
30. Mohellebi H, Kheddar A, Espié S. Adaptive haptic feedback steering wheel for driving simulators. *IEEE Trans Veh Technol*. 2009;58(4):1654–1666.
31. Liu W, Zhang H, Duan B, Yuan H, Zhao H. Vision-based real-time lane marking detection and tracking. In: *11th International IEEE Conference on Intelligent Transportation Systems, 2008*. 2008:49–54.
32. Lim KH, Seng KP, Ngo ACL, Ang LM. Real-time implementation of vision-based lane detection and tracking. In: *International Conference on Intelligent Human–Machine Systems and Cybernetics, 2009, volume 2*. 2009:364–367.
33. Meuter M, Muller-Schneiders S, Mika A, Hold S, Nunny C, Kummert A. A novel approach to lane detection and tracking. In: *12th IEEE International Conference on Intelligent Transportation Systems, 2009*. 2009:1–6.

34. Nieto M, Cortés A, Otaegui O, Arróspide J, Salgado L. Real-time lane tracking using Rao–Blackwellized particle filter. *Journal of Real-Time Image Processing*, 2016;11(1):179–191.
35. Vacek S, Schimmel C, Dillmann R. Road-marking analysis for autonomous vehicle guidance. In: *3rd European Conference on Mobile Robots*. 2007.
36. Dahlkamp H, Kaehler A, Stavens D, Thrun S, Bradski GR. Self-supervised monocular road detection in desert terrain. In: *Robotics: Science and Systems*. 2006.
37. Ma B, Lakshmanan S, Hero AO. Simultaneous detection of lane and pavement boundaries using model-based multisensor fusion. *IEEE Trans Intell Trans Syst*. 2000;1(3):135–147.
38. Laganière R. *OpenCV 2 Computer Vision Application Programming Cookbook: Over 50 Recipes to Master This Library of Programming Functions for Real-Time Computer Vision*. Birmingham, UK: Packt Publishing; 2011.
39. Bradski G. The opencv library. *Dr Dobb's J Softw Tools*. 2000;25(11):120–126.
40. Giachetti A, Campani M, Torre V. The use of optical flow for road navigation. *IEEE Trans Robot Autom*. 1998;14(1):34–48.
41. Barbosa R, Silva J, Junior MM, Gallis R. Velocity estimation of a mobile mapping vehicle using filtered monocular optical flow. In: *International Symposium on Mobile Mapping Technology, volume 5*. 2007.
42. Grabe V, Bulthoff H, Giordano P. On-board velocity estimation and closed-loop control of a quadrotor UAV based on optical flow. In: *IEEE International Conference on Robotics and Automation*. 2012:491–497.
43. Chaumette F, Hutchinson S. Visual servo control, Part I: Basic approaches. *IEEE Robot Automat Mag*. 2006;13(4):82–90.
44. Farnebäck G. Two-frame motion estimation based on polynomial expansion. In: *Image Analysis: 13th Scandinavian Conference, SCIA 2003 Halmstad, Sweden. Lecture Notes in Computer Science*, vol 2749. Berlin: Springer; 2003:363–370.
45. Toibero J, Soria C, Roberti F, Carelli R, Fiorini P. Switching visual servoing approach for stable corridor navigation. In *IEEE International Conference on Advanced Robotics*. 2009:1–6.
46. Vassallo RF, Schneebeli HJ, Santos-Victor J. Visual servoing and appearance for navigation. *Robot Autonom Syst*. 2000;31(1–2):87–97.
47. Ma Y, Soatto S, Kosecka J, Sastry SS. *An Invitation to 3-D Vision: From Images to Geometric Models*. Berlin: Springer-Verlag; 2003.
48. Hogan N. Impedance control—an approach to manipulation. I - Theory. II - Implementation. III - Applications. *J Dyn Syst Meas Control B*. 1985;107:1–24.
49. Vaillant J, Kheddar A, Audren H, et al. Multi-contact vertical ladder climbing with an HRP-2 humanoid. *Autonom Robot*. 2016;40(3):561–580. https://doi.org/10.1007/s10514-016-9546-4
50. Oriolo G, Paolillo A, Rosa L, Vendittelli M. Humanoid odometric localization integrating kinematic, inertial and visual information. *Autonom Robot*. 2015:40(5):1–13. https://doi.org/10.1007/s10514-015-9498-0.
51. DARPAtv. Team AIST-NEDO driving on the second day of the DRC finals. Go at min. 17:20 https://youtu.be/s6ZdC_ZJXK8.

SUPPORTING INFORMATION

Additional Supporting Information may be found online in the supporting information tab for this article.

How to cite this article: Paolillo A, Gergondet P, Cherubini A, Vendittelli M, Kheddar A. Autonomous car driving by a humanoid robot. *J Field Robotics*. 2018;35:169–186. https://doi.org/10.1002/rob.21731